ADVANCED OPTICAL MATERIALS

NEGATIVE INDEX MATERIALS

J. A. Rogers, D. Chanda, and co-workers use a nanotransfer printing technique to fabricate large-area visible 3D negative index metamaterials. Alternating silver and dielectric layers are printed over a large area on a flexible substrate, and deposition conditions are introduced such that nearly ideal geometries with excellent optical properties are obtained.

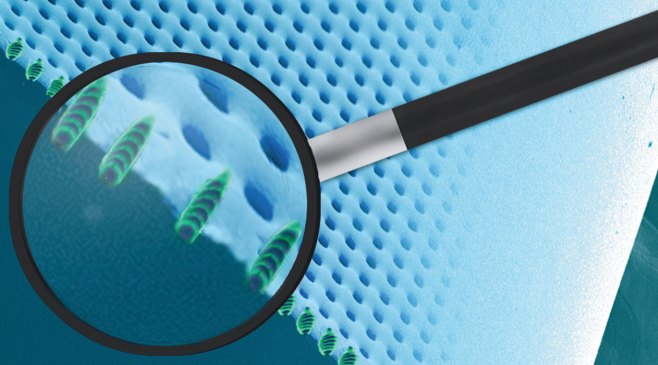

WILEY-VCH

Materials Selections and Growth Conditions for Large-Area, Multilayered, Visible Negative Index Metamaterials Formed by Nanotransfer Printing

Li Gao, Youngmin Kim, Abraham Vazquez-Guardado, Kazuki Shigeta, Steven Hartanto, Daniel Franklin, Christopher J. Progler, Gregory R. Bogart, John A. Rogers, and Debashis Chanda**

Negative index metamaterials (NIMs) are engineered structures that exhibit negative permeability and permittivity. From early demonstrations in the microwave[1,2] and terahertz[3,4] regimes, to more recent work at optical wavelengths,[5–9] designs have evolved from split-ring and U-shaped resonators to metallic cut-wire pairs and dielectric-metal multilayers in open mesh (i.e. fishnet) layouts. This last geometry represents a multilayered construct that not only allows low loss operation at near infrared (NIR) and visible wavelengths, but is also compatible with large area fabrication strategies based on nanotransfer printing (nTP).[10] A critical step in this type of fabrication involves collimated physical vapor deposition (PVD) of alternating layers of metals and dielectrics onto substrates with features of relief that define the fishnet layouts. Detailed mechanisms for film growth depend strongly on materials properties, such as surface mobility, sticking coefficient, crystallinity and grain structure[11,12] and on conditions for deposition, such as rate and base pressure. A behavior of particular relevance here is that the films grow often in a direction that is not entirely perpendicular to the patterned substrate surface (stamp), even for normally incident flux of material. As a result, angled sidewall profiles develop at the edges of deposits near features of relief on the substrate. Although such effects can be useful in the fabrication of silicon nanodome arrays,[13] Spindt-type field emitters,[14,15] nanocones of metals with sharp tips[16] and other related structures, they can be detrimental in the fabrication of metamaterials by nTP. For the case of NIMs that consist of multilayer stacks of silver (Ag)/magnesium fluoride (MgF_2) formed by nTP for operation in the NIR, the sidewall slopes are ~6–12°[10] depending on deposition conditions. This value is comparable to or slightly larger than those observed in otherwise similar structures formed by traditional focused ion beam machining techniques.[9] This angle can be included explicitly in the design and modeling steps, to enable NIMs with excellent and predictable transmission values, with high figures-of-merit for near-IR operations.[10] For operation in the visible, however, the required dimensions of the openings in the fishnet structures can be as small as 200 nm.[17–19] As shown subsequently, in such cases, angular growth can lead to substantial or even complete elimination of the fishnet geometry at the top surfaces of the multilayer stacks. In the following, we explore aspects of PVD growth in previously reported materials for multilayered fishnet NIMs, and introduce alternative dielectrics and deposition conditions that enable nearly ideal geometries by nTP. Demonstrations include large-area, uniform NIMs with excellent characteristics in the visible range, along with modeling results that capture the key behaviors.

Figure 1 provides schematic illustrations of the key steps for fabricating multilayered NIMs by nTP, as implemented here. A silicon wafer with a square array of periodic holes (period, *P*, edge-to-edge separation, *W*, and depth, *H*) serves as a stamp which appears in Figure 1a. The schematic shows the top view of fishnet features of relief and the cross sectional view of this relief cut at the red dash line. Electron-beam evaporation forms multilayer stacks of metals and dielectrics (Figure 1b) on the top and bottom regions of relief, with negligible deposition on the sidewalls. Transfer of material from the top regions to a target substrate, here facilitated by a photocurable polymer as an adhesive, completes the process (Figure 1c). Previous multilayered fishnet NIMs formed by nTP exploited Ag as the metal and MgF_2 as the dielectric,[10] due to their favorable plasmonic properties and established uses in optical coatings, respectively. Although Ag deposited by electron-beam evaporation with a material flux collimated in a direction perpendicular to the substrate surface grows in a nearly vertical fashion, MgF_2 exhibits angular growth with columar grain structure.[10] This latter behavior defines the overall growth profiles of the Ag/MgF_2 multilayers. Figure 1b illustrates the key parameters: the angular profile of the growth, θ, and the characteristic widths at

L. Gao, Dr. Y. Kim, Dr. K. Shigeta, S. Hartanto, Prof. J. A. Rogers
Department of Materials Science and Engineering
Frederick Seitz Materials Research Laboratory
Beckman Institute for Advanced Science and Technology
University of Illinois at Urbana-Champaign
Urbana, IL, 61801, USA
E-mail: jrogers@illinois.edu
Dr. G. R. Bogart
Sandia National Laboratories
Albuquerque, New Mexico, USA
C. J. Progler
Photronics Inc.
Allen, TX, 75013, USA
A. Vazquez-Guardado, D. Franklin, Prof. D. Chanda
NanoScience Technology Center
and College of Optics and Photonics (CREOL)
University of Central Florida
Orlando, FL, 32826, USA
E-mail: debashis.chanda@creol.ucf.edu

DOI: 10.1002/adom.201300356

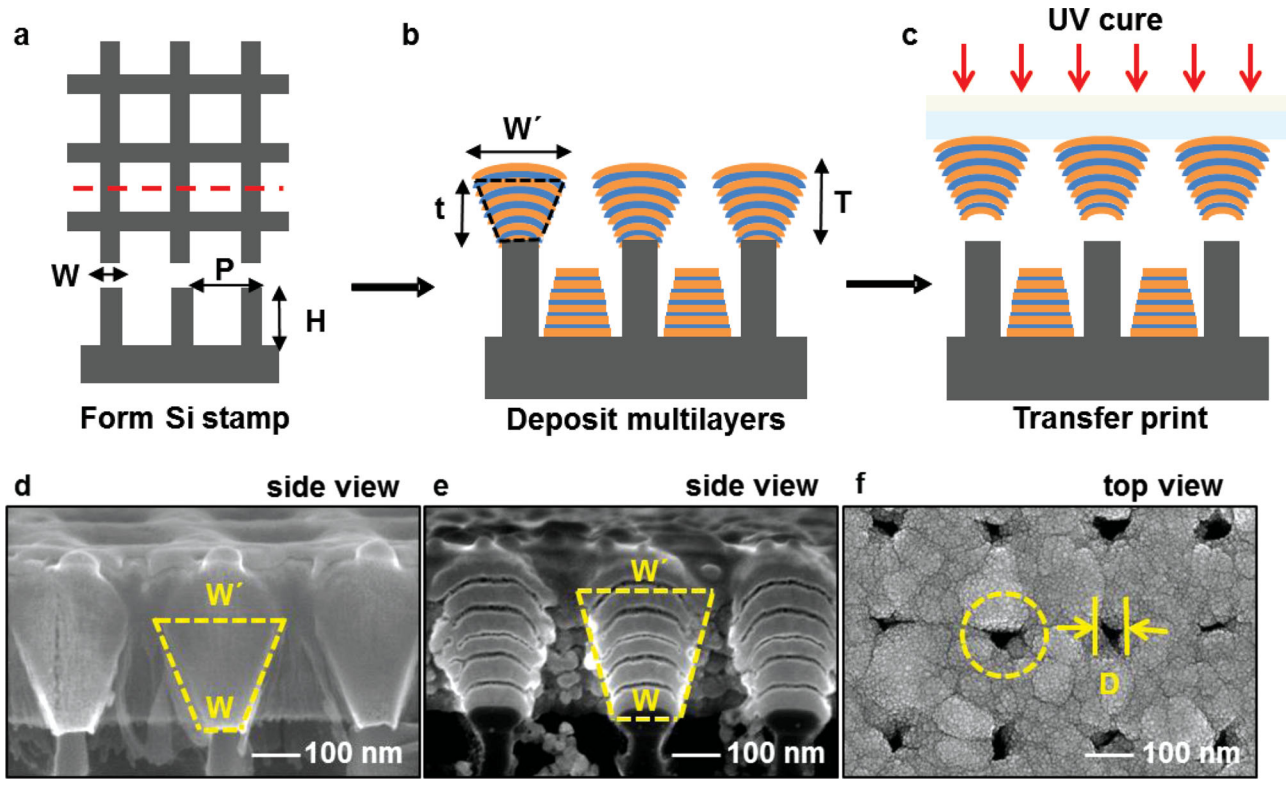

Figure 1. Schematic illustration of steps for fabricating multilayered fishnet NIMs by nanotransfer printing. Top and Cross sectional views of (a) a silicon stamp made by nanoimprint lithography and etching, (b) this stamp after physical vapor deposition of alternating metal and dielectric films, (c) after transfer of the surface multilayer stacks onto a glass substrate coated with a photocurable polymer. Scanning electron micrographs of (d) cross sectional image of a layer of MgF_2 (300 nm) deposited by eleactron-beam evaporation onto a silicon stamp, (e) cross sectional image of alternating layers of Ag (35 nm) and MgF_2 (15 nm) on a silicon stamp, with total thickness ~300 nm, (f) top view of the stamp after deposition shown in (e). The dashed yellow boxes in (d) and (e) show the large angular profiles that develop in the films. The dashed yellow circle in (f) indicates the diameter of the periodic holes on the stamp before deposition.

the bottom, W, and top, W', of a multilayer stack with trapezoid height t. The thickness, T, corresponds to the distance from the base to the highest point on the top surface. The thickness-averaged value of θ is, therefore, simply given by $\tan\theta = (W' - W) / 2t$. For purposes of fabricating fishnet NIMs by nTP, the ideal stack should have $\theta = 0$. All observations in real systems show $\theta > 0$, dominated by angular growth in the dielectric material. Figure 1d-f presents scanning electron microscope (SEM) images of cross sectional and top views of films and multilayers deposited onto silicon stamps with $P = 300$ nm. Figure 1d corresponds to single layer of MgF_2 with $T \sim 300$ nm, where angular growth is evident, i.e., $W \sim 77\pm2$ nm and $W' \sim 228\pm6$ nm, $t \sim 219\pm3$ nm, with $\theta \sim 19.1°\pm0.6°$. Similar studies indicate that θ for Ag is close to zero.[10] This behavior in angular growth of MgF_2 directly affects the geometry of multilayer stacks of Ag (35 nm) / MgF_2 (15 nm) (Figure 1e), where $t \sim 224\pm3$ nm, $W \sim 117\pm3$ nm, $W' \sim 249 \pm 15$ nm, and $\theta \sim 15.3°\pm1.6°$. Here, the diameters (D) of the holes in the fishnet evaluated at the top surface of the deposited multilayers are smaller than the value set by the geometry of the stamp, i.e. ~ 220 nm, and exhibit a large variance, i.e. between 25 nm and 85 nm (Figure 1f). The values of θ, inferred from D, t and the geometry of the stamp, lie within the range of 16°-23° which is somewhat larger, but comparable to, those determined from the cross sections. Although these effects can be manageable in fishnets with relatively large geometries for operation in the IR and NIR,[10] they severely limit designs in the visible, where the period of the fishnet can be in the range of 300 nm or less. These dimensions derive from linear scaling between surface plasmon induced light transmission and structure period.[17–19] For instance, the structures of Figure 1 have an optical transmission of less than ~1% at a wavelength, $\lambda = 650$ nm, due mainly to small values of D. Experiments show that control over physical collimation and other examined conditions associated with deposition offers only limited utility in reducing θ. In our setups, the source for evaporation has a diameter of ~2.5 cm, and the distance from source to sample is ~60 cm; for a sample size of ~2 cm placed perpendicular to the source, the incident material flux front has alomost zero angular distribution over $W \sim 117 \pm 3$ nm linewidth. Further efforts to enhance the degree of collimation using tubes placed between the source and sample dramatically reduce the deposition rates, but without significant benefits in angular growth (Figure S1). Other techniques, such as ion beam assisted electron-beam deposition, also do not decrease θ appreciably (Figure S2). (We note that θ can depend slightly, although not significantly, on the geometry of the relief on the substrate. See Figure S3.) Other inorganic dielectrics with suitable optical properties, such as silica[14] and alumina,[17,18] exhibit similar

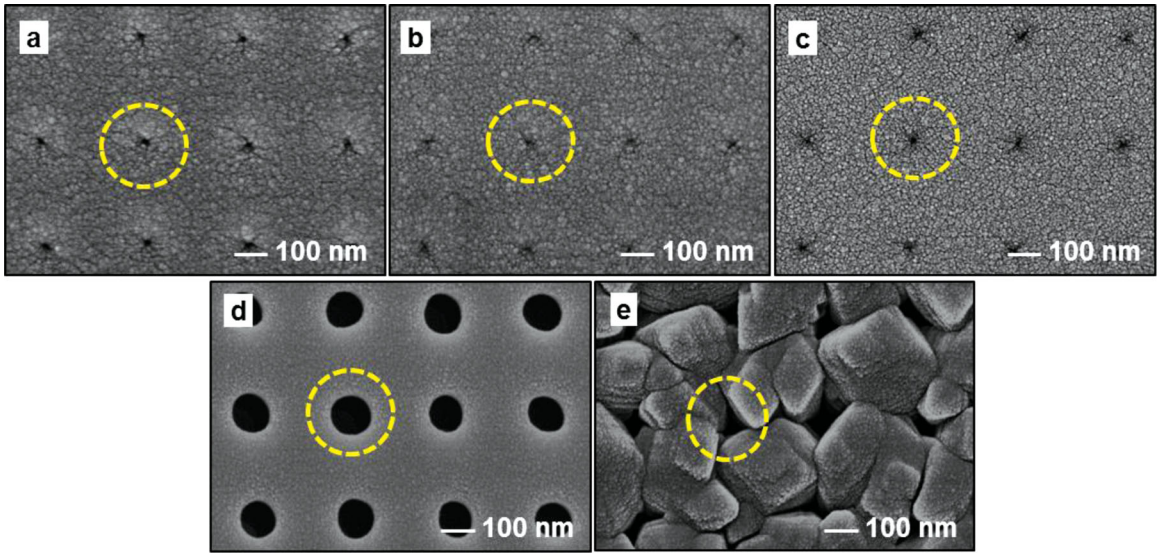

Figure 2. Top view scanning electron micrographs of silicon stamps after deposition of various dielectric materials. (a) Al_2O_3 (340 nm; electron-beam evaporation), (b) SiO_2 (300 nm; electron-beam evaporation), (c) TiO_2 (320 nm; electron-beam evaporation), (d) MG 5 5' 6 6'-tetrahydroxy-3 3 3' 3'-tetramethyl-1 1'-spirobisindane (350 nm; thermal evaporation), and (e) pentacene (300 nm; thermal evaporation). The dashed yellow circles illustrate the diameters of the periodic holes on the stamps before deposition.

behavior. Organic small molecule materials, many of which can be thermally evaporated, represent alternatives.

Figure 2 provides top view SEM images of stamps coated with various candidate materials, including alumina (Al_2O_3; T~ 340 nm; electron-beam evaporation) (Figure 2a), silica (SiO_2; T~ 300 nm; electron-beam evaporation) (Figure 2b), titania (TiO_2; T~ 320 nm; electron-beam evaporation) (Figure 2c), a molecular glass (MG: 5 5' 6 6'-tetrahydroxy-3 3 3' 3'-tetramethyl-1 1'-spirobisindane; T~ 350 nm; thermal evaporation) (Figure 2d) and pentacene (T~ 300 nm; thermal evaporation) (Figure 2e) (organic materials like MG and pentacene were deposited thermally to avoid electron-beam chamber contamination). The results clearly show that only MG yields deposits with $W \sim W'$. Specifically, the inferred values of θ from the images of Figure 2 are: ~25° for Al_2O_3;~30° for SiO_2; ~25° for TiO_2; ~3° for the MG. The θ for pentacene is large, but difficult to estimate due to the grain structures. Such behaviors are qualitatively consistent with previous observations that dielectric materials such as SiO_2 and Al_2O_3 with polycrystalline morphologies tend to grow with large angles on structured surfaces.[14,17,18] The results of Figure 2 suggest that thermally evaporated MG systems[20,21] provide an attractive class of dielectric for NIMs formed by nTP, likely due to their lack of grain structure and non-columnar growth. Cross sectional and top view SEM images in **Figure 3** provide additional evidence that θ is ~2°, not only for a different MG but also for multilayer stacks with Ag. (The slight negative angle observed near the top of the stack arises from the focused ion beam preparation techniques used to enable the cross sectional views.) Figure 3a shows that with a MG thickness $T \sim 300$ nm, where $t \sim 220$ nm, W~110 nm and W'~130 nm, θ ~2.2 ± 0.2°. A multilayer stack of Ag/MG yields a even slightly smaller angle (Figure 3b), where t~205 nm, W~ 115 nm, $W' \sim 125$ nm, and $\theta \sim 1.4 \pm 0.3°$. For this geometry, the hole diameter decreases from the base to the top, from ~185 nm to ~159 nm (Figure 3c). (We note that the value of θ inferred from D is ~3.5°). To ensure suitablity of MG as a good optical dielectric

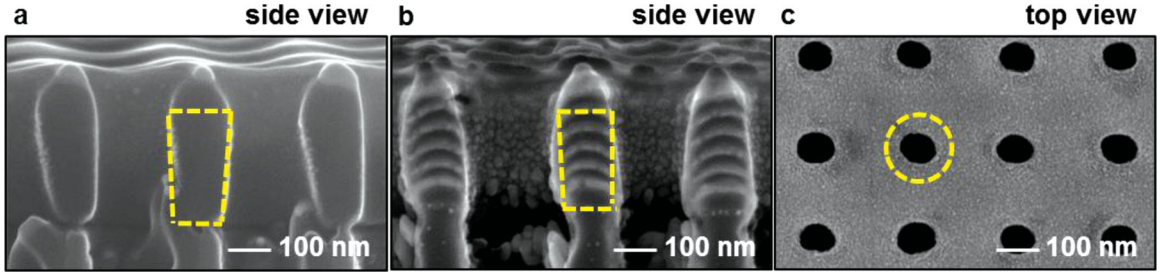

Figure 3. Cross sectional and top view scanning electron micrographs illustrating aspects of using MG (alpha, alpha, alpha'-tris(4-hydroxyphenyl)-1-ethyl-4-isopropylbenzene) as the dielectric. (a) Cross sectional image of a layer of MG (300 nm) deposited by thermal evaporation onto a silicon stamp, (b) cross sectional image of alternating layers of Ag (35 nm) and MG (15 nm) on a silicon stamp, with a total thickness ~280 nm, (c) top view of the stamp after deposition shown in (b). The dashed yellow boxes in (a) and (b) show the slight angular profiles that develop in the films. The dashed yellow circle in (c) indicates the diameter of the periodic holes on the stamp before deposition.

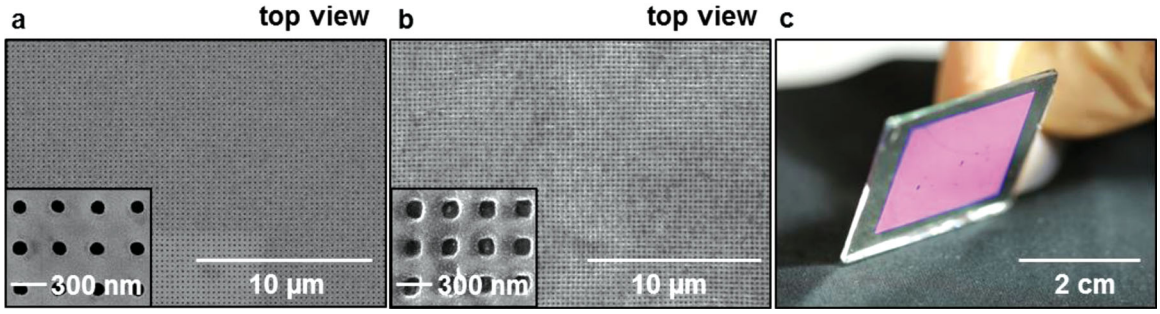

Figure 4. Scanning electron micrographs of large area fishnet NIMs comprised of 11 alternating layers of Ag and MG (alpha, alpha, alpha'-tris(4-hydroxyphenyl)-1-ethyl-4-isopropylbenzene). (a) Top view on the surface of a silicon stamp with an enlarged view as the bottom left inset, (b) top view after transferred to a glass substrate by nTP with an enlaregd view as the bottom left inset, (c) picture of a representative sample, which covers an area of ~4 cm^2.

we performed spectroscopic ellipsometry and experimentally obtained refractive indices (n, κ) which verifies almost no absorption loss over the visible band (Figure S4) and closely matches with previously reported (n, κ) values of such materials.

Deposits like those of Figure 3 can be transferred, by nTP, to a target substrate to complete the fabrication. Here, a layer of a liquid prepolymer (Norland, NOA 63) spin-casted onto a glass plate ensures strong adhesion and high fidelty in the transfer. Photocuring the prepolymer by passing ultraviolet light through the glass and then removing the stamp yields a high quality NIMs structure, without observable defects. **Figure 4** shows large area SEM images of Ag/MG multilayer stacks on a stamp (Figure 4a) and transferred to NOA/glass (Figure 4b). NIMs with macroscopic sizes (~4 cm^2), limited only by the available overall dimensions of the stamp, and with uniform properties are routinely possible (Figure 4c). Optical measurements indicate, however, low transmission in the range of wavelengths of interest, i.e., less than 1% at λ = 650 nm, as can be seen in **Figure 5**a. This low transmission is a direct consequence of the small θ because, in the absence of angular growth, the incident flux of Ag can lead to formation of grains and particles on the sidewalls of the multilayer stacks especially when deposited with thermal evaporation. The effect is visible in Figure 3b. Such deposits can electrically short adjacent Ag layers in the stack, thereby diminishing the excitation of strong magnetic responses that underpin the behavior in the NIMs structure. Immersing the sample in a wet chemical etchant for Ag can reduce or eliminate this problem. For etching times between 15 s to 30 s, the peak transmission increases from 18% to 40%, as shown in Figure 5b. Beyond 30 s, the etchant begins to remove significant amounts of Ag from the multilayer stacks themselves. The excessive removal of Ag causes damage to the desired metal–dielectric–metal LC resonant circuit and the electro-magnetic resonance diminishes and consequently less light transmits out of the structure, thereby leading to a decrease in transmission from 23% to 12% for times of 45 s and 60 s, respectively.

Comparing experimental and finite difference time domain (FDTD) results enables extraction of the effective optical properties of the NIMs. It has been firmly established in the optics community that full-vectorial FDTD prediction of index is sufficiently accurate to experimental observations.[22–24] Interferometric measurements to verify FDTD predictions of negative refractive index have been previously demonstrated for similar fishnet metamaterials.[9,25] Transmission and reflection spectra are calculated using experimental parameters for the printed multilayered NIMs structures, with commercial FDTD software package (Lumerical FDTD, Lumerical Solutions Inc.). A Drude model was used for the dielectric parameters of silver in the FDTD simulation, with plasma frequency 9.0 eV and scattering frequency 0.054 eV. The scattering frequency is increased by a factor of three compared to that of the bulk silver in order to account for the additional surface scattering loss in fabricated structures.[26] These simulation results were used to retrieve the impedance (z) and refractive index (n) of the samples. The retrieval exploited effective medium approaches, as described elsewhere.[22–24] For calculation, we use W = 120 nm, W' = 140 nm and T = 285 nm, with θ = 2° respectively. Optical characterization reveals a broadband transmission peak of 40.1% at 802 nm after an etching time of 30 s. The results exhibit good agreement with FDTD prediction (**Figure 6**a). The origin of the shoulder at around 0.6 μm is due to the partial infiltration of polymer inside the open hole of

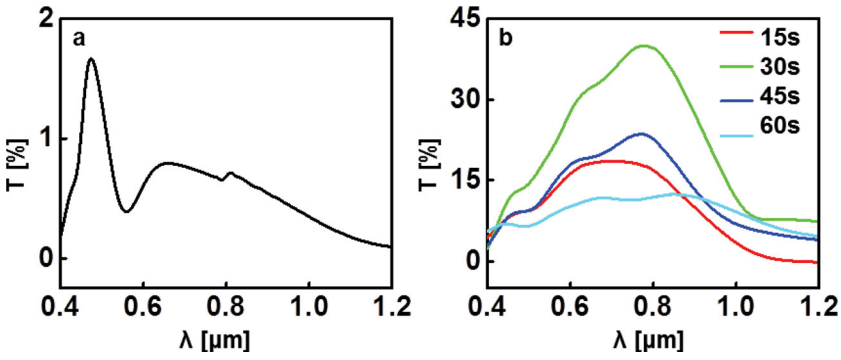

Figure 5. Transmission properties for (a) a stack of 11 alternating layers of Ag and MG (alpha, alpha, alpha'-tris(4-hydroxyphenyl)-1-ethyl-4-isopropylbenzene) on glass, as transferred by nTP, (b) after wet chemical etching of the Ag for different times.

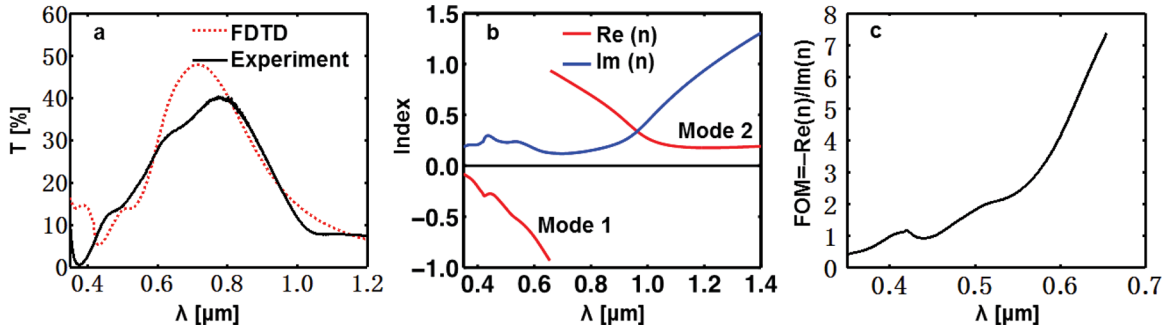

Figure 6. Experimental measurements and simulation results for transmission and refractive indices of Ag and MG (alpha, alpha, alpha'-tris(4-hydroxyphenyl)-1-ethyl-4-isopropylbenzene) NIMs. (a) FDTD predicted and experimentally measured transmission (with 30s Ag etch) for the chosen depth averaged fishnet line width Wav = 130 nm and the corresponding (b) retrieved refractive indices and (c) Figure-of-Merit for P = 300 nm fishnet.

fishnet pattern which causes the plasmonic mode to split due to index contrast across the multilayer stack. Figure 6b shows the real and imaginary components of refractive index extracted by FDTD. The real part of the refractive index is negative from about 350 nm to 654 nm. The effective index of a multilayer metal/dielectric stack differs significantly from their respective bulk values. In the present case the multilayer stacks are comprised of 6 Ag and 5 MG (refractive index = 1.6) alternating layers. The real component of refractive index of "bulk" Ag at around 1 μm is Re(n)~0.1 (Palik Silver) which makes the extracted stack effective index of $Re(n_{eff})$ ~ 0.25 consistent considering 35 nm thick Ag layers verses 15 nm MG layers. Two branches of the Re(n) which are labeled as 'Mode 1' and 'Mode 2' represent two propagating optical modes in the system as previously reported.[6,10] The loss for these types of structures is typically reported in terms of a figure of merit (FOM) defined by –Re(n)/Im(n). The results suggest a high FOM for the visible P = 300 nm Ag/MG NIMs of 7.4 at 654 nm as shown in Figure 6c, consistent with low loss (higher transmission). The good agreement between experiment and FDTD results that assume ideal geometries of the fishnets provides additional evidence of the high structural quality of the samples.

The results described here reveal some important effects of film growth in the formation of fishnet NIMs by large area processing techniques such as nTP. A key finding is that the film growth characteristics in MG systems make them attractive alternatives to more widely explored inorganics for the dielectric layers. The outcomes enable fabrication of multilayered NIMs with excellent operational characteristics in the visible regime and they appear to have implications in other areas of optical application of nanotransfer printing.

Experimental Section

Fabrication of the Silicon Stamp: The silicon was etched using a Bosch process (94 mTorr, etch/passivation: cycle time, 5 s/5 s; RIE power 20 W/0 W, SF6/C4F8 flow rate 35 sccm/110 sccm for constant ICP power of 600 W; etch rate 1 μm/80 s) with SF_6 gas, to a depth of ~500 nm. A layer of photoresist patterned by soft nanoimprint lithography served as the resist. Exposure to C_4F_8 in an ICP-RIE system (STS Inc., RIE power = 0 W, ICP power = 600 W, 15 s, chamber pressure = 94 mTorr, C_4F_8 flow rate 110 sccm) formed a cross-linked polymer on the surface of the silicon to facilitate release in the transfer process by reducing the degree of adhesion between the deposited multilayer stacks and the substrate.

Collimated Deposition of Multilayer Stacks: Multilayer stacks of Ag and MgF_2, and single layers of MgF_2, Al_2O_3, SiO_2, and TiO_2 were deposited using a six-pocket electron-beam evaporation system (AJA International). The sample was mounted close to the center of the dome in the chamber; where the distance between the sample (~2 cm) and source (~2.5 cm) was maximized (~60 cm). The angle between the sample and source was estimated to be less than 5°. Due to the evaporation profile and the spherical dome shape, the incident flux was considered to be uniform over the 2 cm × 2 cm sample area. During deposition of Ag, MgF_2, Al_2O_3, SiO_2 and TiO_2 the average base pressures and growth rates were 1×10^{-8} Torr and 0.1–0.15 nm/s, respectively. The chamber pressure increased by about one order of magnitude during evapporation for most dielectrics except for titania, where the increase was more than two orders of magnitude. Experiments with physical collimators involved a Temescal (FC-1800) six-pocket electron-beam evaporation system, with the sample at one end of a cylindrical metal tube whose other end aligned to the source. The chamber geometry and sample orientation were similar to AJA International electron-beam evaporation system. Sequential thermal evaporation formed stacks of Ag and the MG alpha, alpha, alpha'-tris(4-hydroxyphenyl)-1-ethyl-4-isopropylbenzene with a base pressure of 1.0×10^{-6} Torr and rate 0.05–0.1 nm/s using a thermal evaporator (TCI International). The other MG material, 5 5′ 6 6′-tetrahydroxy-3 3 3′ 3′-tetramethyl-1 1′-spirobisindane, was deposited in similar fashion. Pentacene was deposited at 0.03–0.05 nm/s. All samples were mounted perpendicular to the flux in the thermal evaporator. The distance between the sample (~2 cm) and source (~1 cm) was ~50 cm and the angle between them was less than 2°. A 20 nm thick layer of SiO_2 deposited by electron-beam evaporation (AJA International) on the top layer of Ag served as a resist to wet etching of the Ag from the sidewalls.

Removing Excess Ag by Wet Etching: A mixture of sodium thiosulfate (anhydrous, 1.581 g), potassium ferricyanide (0.042 g), potassium hexacyanoferrate (0.329 g) dissolved in DI water (100 ml) served as the etchant. Immersion times were 15, 30, 40, and 60 s, each followed immediately by rinsing in DI water.

Nanotransfer Printing: A liquid pre-polymer to polyurethane (NOA 63, Norland Inc.) spin-casted onto a clean glass plate served as an adhesive. A silicon stamp coated with multilayer stacks was pressed into contact with this substrate. Passing UV light (Osram Sylvania 100 W MV PAR38, power density 8.4 mW/cm^2) through the glass for 1 h cured the NOA into a solid form, to form a strong bond with the multilayer stack. Removing the stamp completed the process.

Optical Measurements: Transmission spectra were collected using Varian Cary 5G UV-Vis-NIR spectrophotometer where the photo-detector is changed right at 800 nm where a small step-like response is always artificially added to the measured spectrum by the instrument. The data

was collected over a slit with a diameter of 2 mm. Transmission spectra were normalized using a glass substrate with cured NOA.

FDTD Simulations: Transmission spectra were calculated using experimental parameters for the printed NIMs structures, with a commercial FDTD software package (Lumerical FDTD, Lumerical Solutions Inc.). A Drude model was used for the dielectric parameters of Ag in the FDTD simulation, with a plasma frequency of 1.37×10^{16} s^{-1} and scattering frequency of 8.5×10^{13} s^{-1}. The scattering frequency was increased by a factor of 3 compared with that of bulk Ag to account for the additional surface scattering loss. The FDTD simulations used averages of transmission separately computed with plane wave sources of TE and TM polarizations, to compare with the unpolarized light used in the spectrometer. These simulations used precise geometries extracted from images obtained in the experiment but without any line edge roughness (LER). The partial infiltration of openings in the mesh structure with adhesive material (NOA) used in the nTP process increases the background refractive index, ns. The effect moves the optical response to higher wavelength range compared to the case with air as the background medium. We used ns ~ 1.4 in the FDTD modeling. The good agreement between experiment and FDTD results, which assume ideal geometries and zero LER, suggests that the observed losses are intrinsic to the materials. Slight variabilities in the dimensions of the structures, the properties of the constituent materials and the levels of control (such as uniformity and edge roughness) associated with the fabrication are the probable causes of the 10–15% overall discrepancy between experimental observation and FDTD simulation.

Supporting Information

Supporting Information is available from the Wiley Online Library or from the author.

Acknowledgements

L. Gao and Y. Kim contributed equally to this work. The work was supported by a grant from the Office of Naval Research. We also gratefully knowledge the contribution of Sandia National Laboratory which is a multi-program laboratory operated by Sandia Corporation, a Lockheed Martin Company, for the United States Department of Energy under contract DE-AC04–94AL85000 in fabricating large area master mask using deep UV lithography (telecom) and electron beam lithography (visible).

Received: August 22, 2013
Revised: October 23, 2013
Published online: December 11, 2013

[1] R. A. Shelby, *Science* **2001**, *292*, 77.
[2] D. Schurig, J. J. Mock, B. J. Justice, S. A. Cummer, J. B. Pendry, A. F. Starr, D. R. Smith, *Science* **2006**, *314*, 977.
[3] T. J. Yen, W. J. Padilla, N. Fang, D. C. Vier, D. R. Smith, J. B. Pendry, D. N. Basov, X. Zhang, *Science* **2004**, *303*, 1494.
[4] O. Paul, C. Imhof, B. Reinhard, R. Zengerle, R. Beigang, *Opt. Express* **2008**, *16*, 6736.
[5] G. Dolling, C. Enkrich, M. Wegener, C. M. Soukoulis, S. Linden, *Opt. Lett.* **2006**, *31*, 1800.
[6] S. Zhang, W. Fan, N. C. Panoiu, K. J. Malloy, R. M. Osgood, S. R. Brueck, *Opt. Express* **2006**, *14*, 6778.
[7] V. M. Shalaev, *Nat. Photonics* **2007**, *1*, 41.
[8] C. M. Soukoulis, S. Linden, M. Wegener, *Science* **2007**, *315*, 47.
[9] J. Valentine, S. Zhang, T. Zentgraf, E. Ulin-Avila, D. A. Genov, G. Bartal, X. Zhang, *Nature* **2008**, *455*, 376.
[10] D. Chanda, K. Shigeta, S. Gupta, T. Cain, A. Carlson, A. Mihi, A. J. Baca, G. R. Bogart, P. Braun, J. A. Rogers, *Nat. Nanotechnol.* **2011**, *6*, 402.
[11] A. G. Dirks, H. J. Leamy, *Thin Solid Films* **1977**, *47*, 219.
[12] M. M. Hawkeye, M. J. Brett, *J. Vac. Sci. Technol. A* **2007**, *25*, 1317.
[13] C. Becker, D. Lockau, T. Sontheimer, P. Schubert-Bischoff, E. Rudigier-Voigt, M. Bockmeyer, F. Schmidt, B. Rech, *Nanotechnology* **2012**, *23*, 135302.
[14] D. N. Hill, J. D. Lee, J. K. Cochran, A. T. Chapman, *J. Mater. Sci.* **1996**, *31*, 1789.
[15] H. Lee, Y. Park, J. Kim, J. Choi, J. Kim, *J. Vac. Sci. Technol. B* **1999**, *17*, 547.
[16] J. M. Kontio, J. Simonen, J. Tommila, M. Pessa, *Microelectron. Eng.* **2010**, *87*, 1711.
[17] S. Xiao, U. K. Chettiar, A. V. Kildishev, V. P. Drachev, V. M. Shalaev, *Opt. Lett.* **2009**, *34*, 3478.
[18] U. K. Chettiar, A. V. Kildishev, H.-K. Yuan, W. Cai, S. Xiao, V. P. Drachev, V. M. Shalaev, *Opt. Lett.* **2007**, *32*, 1671.
[19] G. Dolling, M. Wegener, C. M. Soukoulis, S. Linden, *Opt. Lett.* **2007**, 32, 53.
[20] J. Dai, S. W. Chang, A. Hamad, D. Yang, N. Felix, C. K. Ober, *Chem. Mater.* **2006**, *18*, 3404.
[21] F. Pfeiffer, N. M. Felix, C. Neuber, C. K. Ober, H. W. Schmidt, *Adv. Funct. Mater.* **2007**, *17*, 2336.
[22] D. R. Smith, S. Schultz, P. Markos, C. M. Soukoulis, *Phys. Rev. B* **2002**, *65*, 195104.
[23] X. Chen, T. M. Grzegorczyk, B. Wu, J. Pacheco Jr., J. A. Kong, *Phys. Rev. E* **2004**, *70*, 016608.
[24] D. R. Smith, D. C. Vier, T. Koschny, C. M. Soukoulis, *Phys. Rev. E* **2005**, *71*, 036617.
[25] C. Garcia-Meca, J. Hurtado, J. Marti, A. Martinez, *Phys. Rev. Lett.* **2011**, *106*, 067402.
[26] P. B. Johnson, R. W. Christy, *Phys. Rev. B* **1972**, *6*, 4370.